# Characterization of Wall Temperature Distributions in a Gas Turbine Model Combustor Measured by 2D Phosphor Thermometry

Christoph M. Arndt*, Patrick Nau, Wolfgang Meier

*German Aerospace Center (DLR), Institute of Combustion Technology*
*Pfaffenwaldring 38-40, D-70569 Stuttgart, Germany*

**Corresponding Author, christoph.arndt@dlr.de*

Proceedings of the Combustion Institute 38 (2021), 1867 – 1875.

The original publication is available at www.elsevier.com

https://doi.org/10.1016/j.proci.2020.06.088

**Abstract**

Instantaneous 2D phosphor thermometry was performed on the windows and combustion chamber posts of an optically accessible dual-swirl gas turbine model combustor operated with $CH_4$ at atmospheric pressure. Two phosphors were used in order to measure different surface temperature ranges: YAP:Eu (temperature range 850 K – 1150 K) and YAG:Eu (temperature range 1100 K – 1300 K). Phosphor coatings were applied to the combustion chamber post and to three vertically oriented stripes on one combustion chamber window. Using interpolation, this allowed the determination of the surface temperature of the complete combustion chamber window. Heat losses across the combustion chamber window were determined by measuring the surface temperature on the inner and outer surface of the window. The phosphor coating was illuminated using the fourth harmonic of a Nd:YAG laser, which was formed into a broad light sheet. The spatially resolved, temperature-dependent decay rate of the phosphorescence was measured with a high speed CMOS camera. Three flames with similar flow fields and thermal powers between 22.5 kW and 30 kW and equivalence ratios between 0.63 and 0.83 were studied. Because the flame characteristics including flow field, heat release and temperature distributions were known from previous measurements the interaction between the flame and the surface temperature could be examined. In this way, the different wall temperatures of the flames could be explained.

## Introduction

The design of modern combustion chambers for gas turbines is essentially based on the use of advanced CFD tools, whose verification and further development in turn depends to a large extent on the availability and quality of validation measurements. Detailed investigations on model combustors have contributed considerably to the progress in this field, especially by the application of laser-based measurement techniques [1]. Important quantities for model validation such as flow field, flame temperatures and species concentration, have been documented with good accuracy for a number of test cases [2, 3]. While burner geometry and operating conditions are usually well described in the corresponding data sets, the temperature distributions of the combustion chamber walls are often missing as important boundary conditions. In CFD models, on the other hand, different assumptions for wall temperatures (e.g. adiabatic walls vs. isothermal walls) can lead to different results regarding the flame shape in the simulations [4].

Phosphor thermometry has proven to be a reliable and precise technique for wall temperature measurements in harsh environments and in combustion applications [5, 6]. For this purpose, the surface is coated with a thin phosphorescent layer. After excitation by a light source (preferably a short-pulse laser, with the pulse length being short in comparison to the phosphor decay time), the decay of the phosphorescence signal is recorded. Because quenching reduces the lifetime at higher temperatures, the lifetime is very sensitive to the temperature. Alternatively, the intensity ratio of different emission bands can be used. This approach however is less sensitive and prone to systematic errors. Most studies use photomultiplier tubes (PMTs) to record the decay rate. This allows only point measurements and long measurement times are necessary to cover for example a complete combustor wall. Two dimensional measurements can not only enable shorter measurements times, but also a better observation of transient effects. Most applications of 2D phosphor thermometry use the intensity ratio approach [7, 8], especially for measurements of gas temperatures, where phosphor particles are seeded into the flow [9-11].

An early approach of Omrane et al. for temporally resolved lifetime 2D phosphor thermometry relied on a framing camera with eight independent detectors [12]. The availability of high-speed cameras simplifies the experimental setup, data evaluation and accuracy, because no individual pixels must be overlapped [13, 14].

In the current study, phosphor thermometry was applied to a dual-swirl gas turbine model combustor (GTMC) that has previously been characterized using different laser techniques [15-18]. The combustion chamber was equipped with quartz windows on four sides and was operated with $CH_4$ at atmospheric pressure. Three different flames with varying thermal power and equivalence ratio were studied. Wall temperature distributions were determined on the inner and outer surface of the windows so that it was also possible to determine the heat flux through the windows. The results of the measurements represent an important supplement to the existing experimental data sets for model

validation. A particular goal of this paper is to associate surface temperatures of the windows with the properties of flames, i.e. to explain the shapes of the temperature distributions with the characteristics of the flames. Therefore, the distributions of the flow field, the heat release and the flame temperature were analyzed with the main focus on the near-surface regions. In this way, differences in the wall temperature distributions of three investigated flames could be attributed to the differences of the flame shapes. Because the surface temperatures cover a broad range from 850 K – 1350 K, a combination of phosphors was necessary. Using a high-speed CMOS camera with a frame rate of 775 kHz, it was possible to measure decay rates from 3 ms down to 1 µs. Thus a broad dynamic range comparable to a conventional PMT setup could be covered.

## Experiment and Data Evaluation

SFB606 GTMC

A schematic of the burner, termed SFB606 GTMC is shown in Figure 1. Details on the geometry can be found in the literature [15, 17], and only a brief overview is provided here.

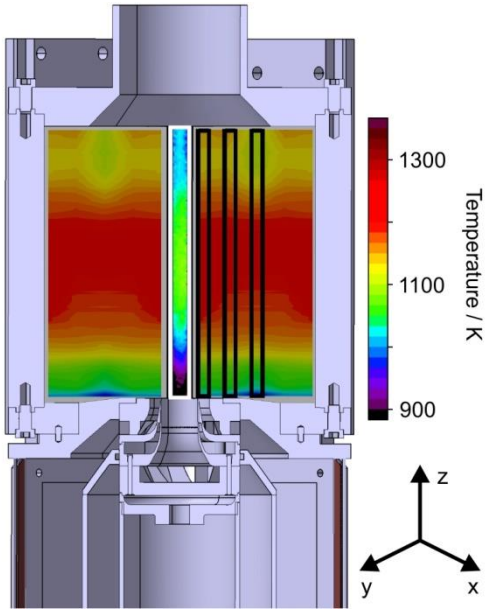


*Figure 1. Schematic of the SFB 606 dual swirl gas turbine model combustor. Color coded are the measured wall temperatures for flame B. The projection in this figure is chosen in such a way that one looks onto the windows at an angle of 45° and thus a post appears in the center of the picture. The measurement regions on the windows are marked by the black rectangles and the measurement region on the combustion chamber post by a white rectangle. Temperatures between the measurement regions were linearly interpolated and the resulting temperature fields were mirrored along the symmetry axis.*

The vertically arranged combustion chamber has a cross section of 89 x 89 $mm^2$ and a height of 112 mm. Air is supplied to the combustion chamber via two concentric, co-rotating swirlers, each being fed through a separate plenum chamber. The mass flow to each swirler can be controlled independently, allowing to set the air split ratio $L$ (defined as the mass flow ratio between the outer and inner air swirler). For the current study, the air split ratio was fixed at $L = 1.6$, corresponding to equal pressure loss across both swirlers.

Fuel is injected through a ring of 60 holes (0.5 mm diameter each) located in the inner air nozzle, 12 mm below the nozzle exit. This results in a partial ("technical") premixing, before the fuel/air mixture enters the combustion chamber. Three flames were compared. The air mass flow was kept constant while the fuel mass flow was varied, resulting in thermal power and equivalence ratios of the flames between 22.5 kW < $P_{th}$ < 30 kW and 0.63 < $\varphi$ < 0.83, respectively (cf. Table 1).

*Table 1. Operating conditions. $T_{ad}$ is adiabatic flame temperature, $\dot{m}$ are the mass flow rates for air in the inner and outer swirler and for $CH_4$.*

| Flame | $P_{th}$ [kW] | $\phi$ [-] | $T_{ad}$ [K] | $\dot{m}_{air,in}$ [g/min] | $\dot{m}_{air,out}$ [g/min] | $\dot{m}_{CH_4}$ [g/min] |
|---|---|---|---|---|---|---|
| A | 22.5 | 0.63 | 1720 | 283 | 453 | 27 |
| B | 25 | 0.7 | 1837 | 283 | 453 | 30 |
| C | 30 | 0.83 | 2030 | 283 | 453 | 36 |

The combustion chamber offers very good optical access from all four sides and is equipped with several ports for dynamic pressure probes. The coordinate system has its origin in the center of the swirler at the burner exit plane.

Phosphor thermometry

Phosphor coatings were applied to the quartz walls and combustion chamber posts with a mixture of a commercial binder (HPC binder, Zyp coatings) and the phosphor powder (YAP:Eu and YAG:Eu, Phosphor Technology). A mixing ratio of 0.2 g phosphor powder to 1 mL binder was used. The mixture was spray-painted onto the surface with an air brush (Badger 100). Coatings were applied as three 5 mm wide, vertically stripes on the windows at $x$ = 0, 16.5, 33 mm. In comparison to coating the entire window, the partial coating reduces a possible effect on radiation heat loss. Separate windows were used for each phosphor. To increase homogeneity of the coating, several layers were painted on the window and each one was dried with a heat gun. After the coating, the substrates were heated in a furnace at 350°C for 1 h and 1000°C for 1 h. The layer thickness was controlled with a coating thickness gauge (Sauter, TE 1250-0.1FN) to achieve a thickness of about 10 µm. In previous experimental [19] and theoretical [20] studies, only negligible influence on thermal conductivity of the windows and on the measured temperatures was found for thicknesses <20 µm.

The forth harmonic of a Nd:YAG laser (Spitlight 600, Innolas GmbH, 15 Hz repetition rate, 6 ns pulse length, 20 mJ pulse energy at 266 nm) was used for excitation of the phosphors. The laser beam was expanded to a slightly expanding sheet with a cylindrical ($f_1$ = -25 mm) and a spherical lens ($f_2$ = +600 mm) to illuminate an area of 115 x 5 mm$^2$. The laser energy density was approximately 3 mJ/cm$^2$.

Phosphorescence was collected by a high speed CMOS camera (LaVision HSS 8, AOI 128 x 24 pixel, frame rate 775 kHz), equipped with a wide angle lens ($f$ = 12 mm, f/1.4, Computar). The angle between laser sheet and camera was about 30°. A longpass filter with a cut-on wavelength of 600 nm (FELH0600, Thorlabs) was used to block laser radiation and most flame emissions, while transmitting the phosphorescence of both phosphors (peak emission at 615 nm [21]). The camera was triggered

0.28 ms before the laser pulse to quantify the offset intensity. Depending on the decay rate of the phosphor, 600 to 3000 images were recorded after each laser pulse, and typically 200 laser shots were recorded for each flame condition.

Calibration and data evaluation

Calibration measurements were performed in an optical accessible furnace (M104, Heraeus). A coated sample was placed in the furnace and the temperature was increased step-wise. At each furnace temperature, 50 to 100 single shot temperature measurements were performed. The same laser and camera setup was used for the calibration measurements to avoid systematic errors. Instead of the commonly used mono-exponential fit, a bi-exponential non-linear fit was used to determine the decay rate, because of the multi-exponential shape of the phosphorescence decay curves. The fitting window was set from the beginning of the curve until the intensity dropped to 5% of the initial value. The same fitting procedure was used both for the calibration measurements and flame measurements. The measured decay rates at each furnace temperature for both phosphors are shown in Figure 2.

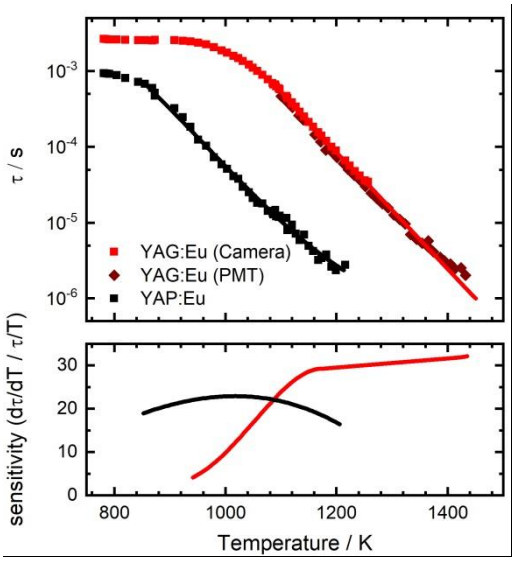


*Figure 2. Calibration measurements (top) and sensitivity (bottom) for the two investigated phosphors YAG:Eu and YAP:Eu.*

The phosphors were chosen to cover a total temperature range of 850 K – 1350 K. A polynomial was fitted to the experimentally obtained decay rates to obtain a calibration formula. Because the maximum temperature that could be achieved with the used oven was 1260 K, the calibration polynomial was linearly extrapolated for YAG:Eu. For comparison, the decay rates obtained in a different furnace using a photomultiplier tube [22] instead of a camera, are also shown, and agree very well with decay rates obtained with the camera. Differences of the gain of the individual pixels were not tested for the current setup. In the literature, deviations on the order of 1% were reported [23]. A pixel-wise evaluation of the surface temperature during the calibration procedure showed no significant pixel-to-pixel variations. The temperature sensitivity of the phosphors is characterized with

the normalized derivative of the calibration polynomial ($d\tau/dT$ / $\tau/T$, with temperature $T$ and decay rate $\tau$). YAP:Eu was used for temperatures between 850 K – 1150 K and YAG:Eu above 1100 K. In these temperature regions the sensitivity factor is above 20 and allows precise temperature measurements.

The minimal measureable decay time is on the order of 1 µs, even if the interframe time is slightly longer. The decay time is defined by a decay to 1/e, and thus also measurement points at a later time in the signal (i.e. with intensities below 1/e) can be used for the fit. For measurements in the calibration furnace with good signal-to-noise ratios, the standard deviation (based on 100 single shots) of a decay time of 1 µs is on the order of 3%. The derived temperature standard deviation is even smaller, depending on the sensitivity of the used phosphor at the specific temperature. A minimum of 4 - 5 data points is required for a robust fit for well-defined conditions (i.e. during calibration). For measurements in reactive flows, more data points are desirable. The exposure time has to be balanced between the signal level and the decay time. A typical minimal exposure time is 1 µs for high speed cameras and sufficient for the here observed decay times. A shorter exposure time (and higher frame rate) typically also enhances the dynamic range of the measurement.

The standard deviation of the decay rate is, especially for the short decay rates, somewhat higher (up to 10%) compared to a conventional PMT setup due to the reduced number of data points. Due to the high temperature sensitivity and the exponential dependence of the decay time on the surface temperature the standard deviation in the temperature is still below 1%. Day-to-day variations in the temperature measurements are below 1% for $T < 1100$ K.

**Results and Discussion**

Characterization of the studied flames

This section provides a short characterization of the three flames examined. Figure 3 compares the mean OH* chemiluminescence (CL) intensity distributions.

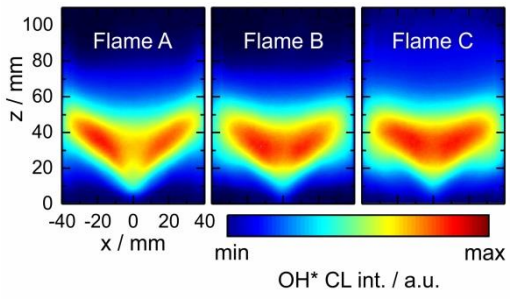


*Figure 3. Averaged OH* chemiluminescence distributions. Each image is normalized to its maximum.*

All flames exhibit a V-shape and the flame base is lifted approximately 8 mm from the burner face plate. With varying thermal power, the axial and radial extent of the flame brush remains similar and extends to axial locations of $z$ = 50 mm. The apex angle of the flame is smaller for flame A in comparison to flames B and C. With increasing $\varphi$ and $P_{th}$, the integrated OH* CL intensity increases, as expected (not visible due to the normalization on the corresponding maximum of each flame). The CL distribution also becomes more homogeneous (higher intensities on the centerline) with increasing $P_{th}$.

Figure 4 shows the mean velocity fields.

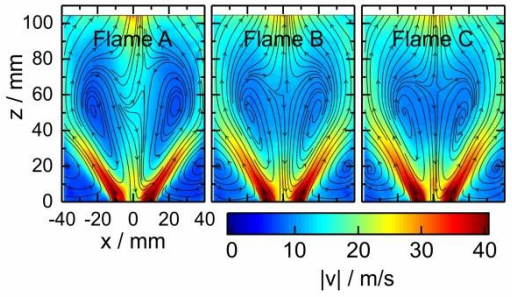


*Figure 4. Mean velocity fields. Shown is the total velocity, and overlaid are the streamlines.*

The similarity between them is not surprising because the air mass flow is the same for the three cases. With increasing thermal power, the velocities in the upper part of the inner recirculation zone become lower while they increase close to the nozzle. The shape of the flow field (apex of the inflow, position of the inner and outer recirculation zone) is almost identical for all three flames. For interpretation of the combustion chamber wall temperatures, the flow field near the walls is of particular interest. The inflowing jet reaches the walls at $z \approx 35$ mm. For $z < 35$ mm and $|x| > 20$ mm, an outer recirculation

zone is visible. For $z > 35$ mm, the flow remains parallel to the wall surface throughout the height of the combustion chamber.

Figure 5 shows the gas temperatures fields inside the combustion chamber, interpolated from pointwise laser Raman measurements. Details on the measurements can be found in [15, 16].

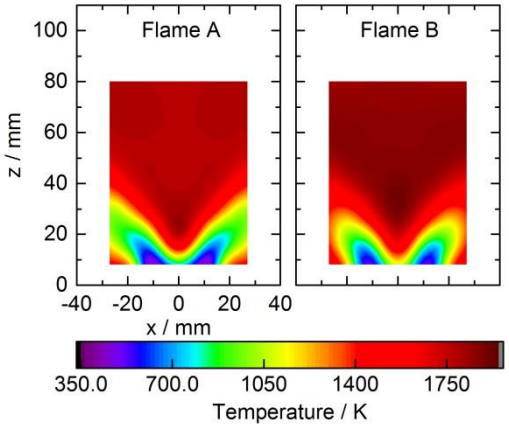


*Figure 5. Gas temperatures $T_{gas}$ (interpolated from pointwise laser Raman measurements) for flame A and B. $T_{gas}$ is not available for flame C.*

Here, measurements were only performed in one half of the combustor, and the results were mirrored in order to get a better overview. Due to the optical arrangement, measurements could not be performed for $x > 27$ mm and $z > 80$ mm. The lowest temperatures of approximately 350 K occur in the inflow region for both cases. For $z > 50$ mm, the flame reactions are complete in the measurement region for both flames and the temperature in the combustion chamber is nearly constant at all radii. Slightly higher temperatures are observed further away from the symmetry axis. The absolute temperatures for flame A are lower than those of flame B due to the lower equivalence ratio and thermal power. Comparing the temperature distributions of the two cases, a much larger region of lower temperatures in the inflow region is present for flame A. This is due to the slower burnout, which is caused by the lower reactivity of the mixture due to lower $\varphi$ and thus lower flame temperature (in comparison to flame B).

Wall temperatures

Sample 2D results of phosphor thermometry for Flame B are shown in Fig. 1. Here, the window regions marked by black rectangles as well as the combustion chamber post (marked by a white rectangle) correspond to the regions where phosphor coatings were applied. On the windows, measurements were performed in three of the marked regions (center of the window, and two offset stripes), and temperatures between those regions were linearly interpolated and the resulting temperature fields were mirrored along the symmetry axis. While the shape of the temperature distribution is similar both on the quartz combustion chamber windows and on the Inconel combustion chamber posts, the temperature on the windows is 100 K – 200 K higher, depending on the operating

condition, due to the higher thermal conductivity of the Inconel combustion chamber posts. The largest temperature differences between combustion chamber posts and windows were observed for the highest thermal power case.

The averaged (typically from 200 single shots) 2D-interpolated temperatures on the inner surface of the combustion chamber windows are shown in Figure 6. Measurements were performed on one half of the windows and were mirrored in order to get a better overview.

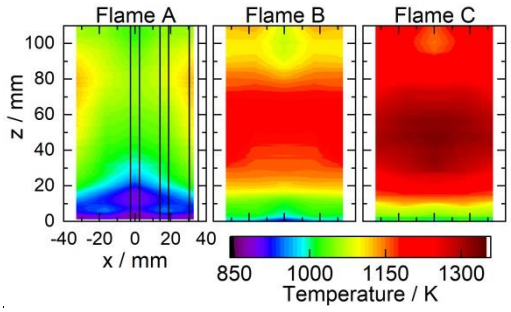


*Figure 6. Interpolated combustion chamber window temperatures on the inner surface of the window for the three flames (mirrored around the symmetry axis). The position of the phosphor coating stripes is marked by the black rectangles.*

For the results presented here, temperature measurements using two different phosphors were performed in order to increase the accessible temperature range. Temperatures below $T_{surf}$ = 1150 K correspond to measurements using YAP:Eu, while temperature above $T_{surf}$ = 1100 K correspond to measurements using YAG:Eu. In the overlapping region, the temperatures of the two phosphors were averaged.

Significant differences are seen between the three distributions. As expected, the flame with the highest $P_{th}$ leads to the highest $T_{surf}$ with a maximum value of 1330 K. However, also the shape of the distributions of flame A and C are different. The distribution for flame C is quite good to follow. From the distributions of CL, velocity and $T_{gas}$ presented above it is obvious that hot combustion products reach the windows with relatively high velocity at $z \approx 50$ mm. Thus, the highest $T_{surf}$ is expected around this location. Because $T_{surf}$ is lower than $T_{gas}$, the gas suffers heat loss on its further way downstream along the window and therefore also $T_{surf}$ decreases slightly. Just above the burner face, the medium level of $T_{surf}$ around 1000 K is explained by the heat delivered by the outer recirculation of hot gas and heat loss at the surfaces. For flame A, in contrast, the highest $T_{surf}$ is observed near the corners at $z \approx 80$ mm. This can be explained by the lower reactivity and longer burnout time of this flame. As can be seen in Figure 3 and partly in Figure 5, it extends a bit further in axial and radial directions compared to the other flames and flame reactions are not complete when the flame first reaches the combustion chamber windows. Since the combustion chamber has a square cross section, the flame gases that flow into the corners have more space (and time) to complete reactions compared to those that flow towards the center of the windows. Therefore the gas reaching the corners has a higher temperature compared to those reaching the center of the windows. Consequently, $T_{surf}$ is also

high near the corners. Also, reacted gas that takes longer to reach the combustion chamber walls has less time for heat loss at the walls. Upstream of the flame region ($z < 20$ mm), the lowest temperatures are observed. Due to the outer recirculation zone, which transports hot gas back to the flame root, the surface temperatures still remain >800 K. For flame A, the lowest temperatures upstream of the flame zone are observed in the center of the window, as explained above. The surface temperature distribution of Flame B lies approximately between those of flames A and C but closer to Flame C.

Figure 7 shows the vertical profiles of the ensemble averaged inner and outer surface temperature along the centerline of combustion chamber window at $x = 0$ mm. A horizontal binning over a 5 pixel range was applied, corresponding to the width of the phosphor stripe.

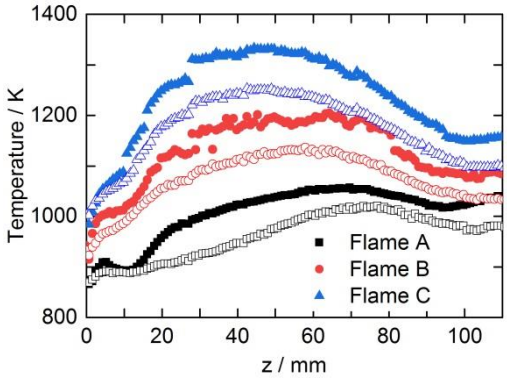


Figure 7. Vertical profiles of the mean value of the inner (closed symbols) and outer (open symbols) surface temperature of the combustion chamber window at x = 0 mm. In the hottest region, the measurement precision is on the order of 3%, typical values in the colder regions are 1%.

First, the temperatures on the inner surface are discussed. Here, two types of temperature profiles are observed. For flame A, the surface temperature increases monotonically after a dip at $z \approx 10$ mm for $z > 20$ mm until it reaches its maximum at $z \approx 75$ mm. A physical explanation for this dip at $z = 10$ mm cannot be given based on the current dataset. Additional measurements, e.g. with an additional phosphor, might help to better understand this phenomenon. The overall shape and monotonically increase of the surface temperature up to $z \approx 75$ mm is due to a comparably low reactivity of the mixture and thus the necessity of long residence times to complete the flame reactions. For flames B and C, the broad temperature maximum is reached around $z = 30$ mm, and remains nearly constant for $z < 80$ mm and $z < 60$ mm for flame B and C, respectively. Here, flame reactions are completed earlier due to the increased reactivity of the mixtures and temperature changes of the gas close to the surface cannot be caused by chemical reactions, but only by heat loss at the walls. Consequently, on the way downstream, the gas temperature decreases, and subsequently also the surface temperature. This effect becomes more clearly visible with increasing thermal power. In addition to the shapes, the absolute temperatures vary between the flame cases. For flame A and C, the difference in peak temperatures is approximately 325 K or 30%.

Discontinuities in the temperature profiles are due to window fouling on the laser entry and detection side (at $z$ = 30 mm), reducing the local laser intensity and the signal-to-noise ratio. Further discontinuities can be observed at the transition from the phosphor overlap region and the regions where the temperature was only determined based on one phosphor ($z$ = 20 – 28 mm and $z$ = 80 – 88 mm for Flame B and $z$ = 10 – 15 mm for Flame C, where averaged temperatures of both phosphors were evaluated). The difference in surface temperatures between the two phosphors is typically < 15 K, and comparable to the day-to-day reproducibility of the measurements. The measurement precision (corresponding to the standard deviation of the single shot measurements) are largest in hottest regions (40 K or 3% for T = 1330 K), typical values in colder regions are on the order of 1%.

The temperatures of the outer surfaces follow the same trend as those for the inner surfaces. The profiles for Flame B and C are similar in shape, with a temperature maximum at $z$ = 60 mm and $z$ = 40 mm, respectively. The temperature difference between the inner and outer surface lies between zero or close to zero for ($z$ < 10 mm) and 80 K at approximately $z$ = 50 mm for flame C. Hence, upstream of the flame base, the heat flux is minimal. For all flames, the highest heat losses, corresponding to the highest temperature differences, occur at approximately $z$ = 50 mm, which is close to the position where the inflowing jet impinges on the wall and hence the highest gas mass flows perpendicular to the wall are expected.

The heat flux density (heat flux $\Phi$ per area $A$) $\Phi/A = -k\,\Delta T/\Delta x$ was calculated using the temperature difference between the inner and outer surface of the window $\Delta T$, the window thickness $\Delta x$ = 1.75 mm and the values for thermal conductivity $k$ of fused quartz from Bityukov and Petrov [24]. To obtain the total heat flux through the windows the heat flux densities were integrated and multiplied with the number of windows (four). The resulting total heat flux is tabulated in Table 2.

*Table 2. Estimated total and relative heat losses through the four windows.*

| Flame | tot. heat flux [kW] | rel. heat flux [%] |
|---|---|---|
| A | 2.2 ± 0.5 | 9.9 ± 2.2 |
| B | 2.5 ± 0.5 | 10.1 ± 2.0 |
| C | 2.9 ± 0.9 | 9.7 ± 2.9 |

The uncertainties of the heat losses were determined using error propagation and the standard deviations of the inner and outer surface temperatures.

While the absolute heat flux increases linearly with the thermal power, the relative heat flux through the windows is more or less identical for all investigated flames (about 10%). Due to the delayed reactions for the case with the lowest equivalence ratio, the highest gas temperatures are reached further downstream. Similarly, the region with the highest heat losses is also further downstream for

Flame A (in comparison to Flame B and C); however the spatially, integrated relative heat loss remains on the same order of magnitude.

## Conclusions

In the current study, the applicability of 2D wall temperature measurements in a gas turbine model combustor using thermographic phosphors was successfully demonstrated. Surface temperatures were measured with high precision on the combustion chamber windows and combustion chamber posts. Three different flames with constant air mass flow and varying fuel mass flow (corresponding to a variation of the equivalence ratio and thermal power) were studied in order to gain information about the influence of different flame shapes and gas temperatures on the window temperature distributions.

The absolute surface temperatures varied strongly with the thermal power and gas temperature. Interestingly, also the shapes of the temperature distributions on the windows exhibited significant differences for the three studied flames. The highest wall temperatures for flame A (lowest $\varphi$) were reached farther downstream in comparison to flame B and C (with higher $\varphi$) and also the lateral temperature profiles were different. In contrast to flames A and B, the flame reactions in flame A were not completed when the flow impinged the combustion chamber wall. Thus the square cross section of the combustion chamber had an influence on the temperature distribution of the windows. Since there is more space and time for the flow to complete reaction on its path to the corners of the combustion chamber, the highest wall temperatures were observed here for flame A, while the temperature in the center of the combustion chamber window was lower. This effect was not present for flames B and C, which featured an increased reactivity due to the higher equivalence ratio.

The heat flux across the combustion chamber windows was estimated by measuring the surface temperature on the inner and outer surface of the combustion chamber. The highest heat fluxes occurred at approximately the same axial location for all three flames, close to the location where the inflowing jet impinges on the combustion chamber wall and hence where the highest flow velocities perpendicular to the combustion chamber walls are expected. The absolute heat flux varied in dependence of the operating condition, the relative heat flux however was independent of the operating condition for the here examined cases.

## Declaration of Competing Interest

None.

## Acknowledgements

The investigations were conducted as part of the joint research program CEC (Siemens Clean Energy Center). The work was supported by the Bundesministerium für Wirtschaft und Energie (BMWi) as per resolution of the German Federal Parliament under Grant No. 03ET7073B.

**References**


[1] International Workshop on the Measurement and Computation of Turbulent Flames (TNF). https://tnfworkshop.org/

[2] A. R. Masri, Partial premixing and stratification in turbulent flames, Proc. Combust. Inst. 35 (2) (2015) 1115-1136.

[3] Y. M. Al-Abdeli, A. R. Masri, Review of laboratory swirl burners and experiments for model validation, Exp. Therm. Fluid Sci. 69 (2015) 178-196.

[4] H. Seliger, M. Stöhr, Z. Yin, A. Huber, M. Aigner, Experimental and Numerical Analysis of FLOX®-Based Combustor for a 3kW Micro Gas Turbine Under Atmospheric Conditions, Proc. ASME Turbo Expo (2017) GT2017-63317.

[5] M. Aldén, A. Omrane, M. Richter, G. Särner, Thermographic phosphors for thermometry: A survey of combustion applications, Prog. Energy Combust. Sci. 37 (4) (2011) 422-461.

[6] J. Brübach, C. Pflitsch, A. Dreizler, B. Atakan, On surface temperature measurements with thermographic phosphors: A review, Prog. Energy Combust. Sci. 39 (1) (2013) 37-60.

[7] M. K. Chyu, Y. C. Hsing, Use of a Thermographic Phosphor Fluorescence Imaging System for Simultaneous Measurement of Film Cooling Effectiveness and Heat Transfer Coefficient, Proc. ASME Turbo Expo (1996) 96-GT-430.

[8] A. L. Heyes, S. Seefeldt, J. P. Feist, Two-colour phosphor thermometry for surface temperature measurement, Optics & Laser Technology 38 (4) (2006) 257-265.

[9] L. Fan, Y. Gao, A. Hayakawa, S. Hochgreb, Simultaneous, two-camera, 2D gas-phase temperature and velocity measurements by thermographic particle image velocimetry with ZnO tracers, Exp. Fluids 58 (4) (2017) 34.

[10] C. Abram, B. Fond, A. L. Heyes, F. Beyrau, High-speed planar thermometry and velocimetry using thermographic phosphor particles, Appl. Phys. B 111 (2) (2013) 155-160.

[11] Z. Yin, B. Fond, G. Eckel, C. Abram, W. Meier, I. Boxx, F. Beyrau, Investigation of BAM:Eu2+ particles as a tracer for temperature imaging in flames, Combust. Flame 184 (2017) 249-251.

[12] A. Omrane, F. Ossler, M. Aldén, Two-dimensional surface temperature measurements of burning materials, Proc. Combust. Inst. 29 (2) (2002) 2653-2659.

[13] T. Kissel, E. Baum, A. Dreizler, J. Brübach, Two-dimensional thermographic phosphor thermometry using a CMOS high speed camera system, Appl. Phys. B 96 (4) (2009) 731-734.

[14] S. Someya, M. Uchida, K. Tominaga, H. Terunuma, Y. Li, K. Okamoto, Lifetime-based phosphor thermometry of an optical engine using a high-speed CMOS camera, Int. J. Heat Mass Transfer 54 (17) (2011) 3927-3932.

[15] C. M. Arndt, M. Severin, C. Dem, M. Stöhr, A. M. Steinberg, W. Meier, Experimental analysis of thermo-acoustic instabilities in a generic gas turbine combustor by phase-correlated PIV, chemiluminescence, and laser Raman scattering measurements, Exp. Fluids 56 (4) (2015) 69.

[16] C. M. Arndt, M. Stöhr, M. J. Severin, C. Dem, W. Meier, Influence of air staging on the dynamics of a precessing vortex core in a dual swirl gas turbine model combustor, 53rd AIAA/SAE/ASEE Joint Propulsion Conference (2017) AIAA 2017-4683.

[17] W. Meier, C. Dem, C. M. Arndt, Mixing and reaction progress in a confined swirl flame undergoing thermo-acoustic oscillations studied with laser Raman scattering, Exp. Therm. Fluid Sci. 73 (2015) 71-78.

[18] C. Kraus, L. Selle, T. Poinsot, C. M. Arndt, H. Bockhorn, Influence of Heat Transfer and Material Temperature on Combustion Instabilities in a Swirl Burner, J. Eng. Gas Turbines Power 139 (5) (2016) 051503.

[19] C. Knappe, M. Algotsson, P. Andersson, M. Richter, M. Tunér, B. Johansson, M. Aldén, Thickness dependent variations in surface phosphor thermometry during transient combustion in an HCCI engine, Combust. Flame 160 (8) (2013) 1466-1475.

[20] C. C. Pilgrim, J. P. Feist, A. L. Heyes, On the effect of temperature gradients and coating translucence on the accuracy of phosphor thermometry, Meas. Sci. Technol. 24 (10) (2013) 105201.

[21] T. Kissel, J. Brübach, M. Euler, M. Frotscher, C. Litterscheid, B. Albert, A. Dreizler, Phosphor thermometry: On the synthesis and characterisation of $Y_3Al_5O_{12}$:Eu (YAG:Eu) and $YAlO_3$:Eu (YAP:Eu), Mater. Chem. Phys. 140 (2) (2013) 435-440.

[22] P. Nau, Z. Yin, K. P. Geigle, W. Meier, Wall temperature measurements at elevated pressures and high temperatures in sooting flames in a gas turbine model combustor, Appl. Phys. B 123 (12) (2017) 279.
[23] V. Weber, J. Brübach, R. L. Gordon, A. Dreizler, Pixel-based characterisation of CMOS high-speed camera systems, Appl. Phys. B 103 (2011) 421-433.
[24] V. K. Bityukov, V. A. Petrov, Optical quartz glass as a reference substance for the thermal conductivity coefficient of partially transparent materials, High Temp. 38 (2) (2000) 293-299.